Immuno-PET Imaging of Engineered Human T Cells in Tumors

Sabine Mall[1], Nahid Yusufi[2], Ricarda Wagner[1], Richard Klar[1], Henrique Bianchi[1], Katja Steiger[3], Melanie Straub[3], Stefan Audehm[1], Iina Laitinen[2], Michaela Aichler[4], Christian Peschel[1,5], Sibylle Ziegler[2], Mona Mustafa[2], Markus Schwaiger[2,5], Calogero D'Alessandria[2], and Angela M. Krackhardt[1,5,6]

Abstract

Sensitive *in vivo* imaging technologies applicable to the clinical setting are still lacking for adoptive T-cell–based immunotherapies, an important gap to fill if mechanisms of tumor rejection or escape are to be understood. Here, we propose a highly sensitive imaging technology to track human TCR-transgenic T cells *in vivo* by directly targeting the murinized constant TCR beta domain (TCRmu) with a zirconium-89 (^{89}Zr)-labeled anti–TCRmu-F(ab')$_2$ fragment. Binding of the labeled or unlabeled F(ab')$_2$ fragment did not impair functionality of transgenic T cells *in vitro* and *in vivo*. Using a murine xenograft model of human myeloid

sarcoma, we monitored by Immuno-PET imaging human central memory T cells (T$_{CM}$), which were transgenic for a myeloid peroxidase (MPO)–specific TCR. Diverse T-cell distribution patterns were detected by PET/CT imaging, depending on the tumor size and rejection phase. Results were confirmed by IHC and semiquantitative evaluation of T-cell infiltration within the tumor corresponding to the PET/CT images. Overall, these findings offer a preclinical proof of concept for an imaging approach that is readily tractable for clinical translation. *Cancer Res; 76(14); 1–11. ©2016 AACR.*

Introduction

Adoptive transfer of T cells genetically modified by T-cell receptors (TCR) specifically recognizing malignant cells is an evolving therapeutic option for cancer patients. Clinical efficacy of TCR-transgenic T cells with specificity for cancer-associated antigens has been demonstrated (1–3), although long-term benefits are currently still limited (4). Novel target structures and TCR recognizing such targets are under intensive investigation. Understanding the *in vivo* behavior of such genetically modified T cells in preclinical models has a high value for optimization of this approach before clinical application. More importantly, clinically applicable imaging technologies for TCR-modified T cells are considered to be critical for an improved comprehension of pharmacodynamics and pharmacokinetics in the clinical context of immunotherapy.

Positron emission tomography (PET) imaging is a noninvasive imaging technology providing advantages due to high spatial and temporal information on cellular distribution with the potential for clinical translation (5). However, most T-cell imaging approaches using PET are far from clinical application and none has been yet clinically approved. This is mainly caused by species-specific tool development in non-humans, the often applied clinically non-significant *ex vivo* labeling procedures providing only short-term information after adoptive T-cell transfer and the negative impact of the labeling on T-cell function (6–10). Promising novel approaches include the usage of reporter genes or antibody derivatives for imaging. Usage of reporter genes such as HSV1-tk has been closest to clinical translation with few patients treated, although technical and regulatory hurdles so far impede broader application (5, 11–15). *In vivo* imaging by Immuno-PET using antibody derivatives for targeting has been already clinically applied, although mainly for delineation of tumors (16). Recently, this technology has been also investigated to track murine T cells by targeting either general T-cell markers as CD4 and CD8 (17–19) or murine monoclonal TCR (20). However, these tools are mouse-specific and cannot be applied in humans. Moreover, the impact of these targeting strategies on T-cell function has not been analyzed so far. Thus, clinically translatable T-cell imaging strategies with high sensitivity and lack of functional impairment are currently missing although urgently needed.

We here take advantage of the introduction of murine sequences within the constant domain of TCR constructs as general optimization strategy for transgenic human TCR (21). This opens the possibility to use an anti-murine TCR monoclonal antibody (aTCRmu; ref. 22) for detection of TCR-transduced human T cells independent of the specificity of the transgenic TCR (23–25). We developed an F(ab')$_2$-fragment–based imaging approach in a xenogenic human myeloid sarcoma model for

sensitive tracking of TCR-transgenic T cells by PET/CT imaging *in vivo*.

Materials and Methods

Primary material and cell lines

Blood from healthy donors was collected for isolation of peripheral blood mononuclear cells (PBMC) after informed consent following requirements of the local ethical board and principles of the Helsinki Declaration. The following cell lines were used: ML2 (The CABRI consortium, obtained in 2004), NSO-IL15 cells (kindly provided by S.R. Riddell in 2011; ref. 26), the TCRαβ-deficient T-cell line Jurkat76 (27), transduced with the CD8 alpha chain (Jurkat76-CD8α; kindly provided by W. Uckert, Molecular Cell Biology and Gene Therapy, Max-Delbrück-Center for Molecular Medicine, Berlin, Germany, in 2007) and the hybridoma H57-597 (HB-218, ATCC, acquired in 2012). All cell lines were routinely analyzed microscopically and tested for Mycoplasma infection (Venor GeM Mycoplasma Detection Kit, Minerva Bio-labs), expression of cell line specifying surface markers, transgene expression, and HLA-typing.

Genetic modification of CD8^{+} central memory T cells and tumor cell lines by retroviral gene transfer

Human CD8^{+} central memory T cells (T$_{CM}$) were isolated from PBMCs and retrovirally transduced with the optimized construct of TCR2.5D6 as described previously (23) and outlined in Supplementary Material. Jurkat76-CD8α cells were transduced with TCR2.5D6 and a cell line with stable transgene expression was generated by single-cell cloning. For *in vivo* depletion analyses, we used a TCR2.5D6 construct linked to near-infrared red protein (iRFP) by a T2A element. ML2 cells were transduced by the HLA-B*07:02 gene linked to enhanced GFP (eGFP). A stable ML2-B7GFP (ML2-B7) cell line was generated by single-cell cloning.

Antibodies, flow cytometry–based assays, and analysis of cytokine secretion

The following antibodies, antibody derivatives, and cell-labeling agents were used: The aTCRmu-IgG and F(ab')$_2$ were prepared from supernatant of H57-597 hybridoma cells using the Protein A-Sepharose (GE Healthcare) and F(ab')$_2$ Preparation Kit (Thermo Scientific Pierce; Supplementary Material). For flow cytometry (LSRII; BD Biosciences), anti-human CD3 (UCHT1), anti-murine-TCRβ-FITC (H57-597; all BD Biosciences), anti-human CD45 (J.33), and anti-human CD5 (BL1a, both Beckman Coulter), the MPO$_5$-specific multimer (23), Annexin-5 (BD Biosciences), and 7-Aminoactinomycine (7-AAD, Sigma-Aldrich) were used. K_d determination and apoptosis assays were performed by flow cytometry (LSRII) as described in the Supplementary Material. Cytokine secretion was analyzed as described previously (23) and outlined in the Supplementary Material.

Tumor model and adoptive T-cell transfer

C.Cg-Rag2[tm1Fwa]Il2rg[tm1Sug]/JicTac (BRG; Taconic) and NOD.Cg-Prkdc[scid] Il2rg[tm1Wjl]/SzJ (NSG; The Jackson Laboratory) were maintained according to the institutional guidelines and approval by local authorities. For depletion analysis, mice were challenged 1 day after intravenous injection of 1.5×10^7 TCR2.5D6-iRFP–transduced T$_{CM}$ (70% iRFP positivity) with 150 µg of aTCRmu-IgG or isotype-IgG and 110 µg of aTCRmu-F(ab')$_2$, or isotype-F

(ab')$_2$ (both corresponding to 500 nmol/L in assumption of a 2-mL blood volume). To analyze T cells at the tumor site, 1×10^7 ML2-WT and ML2-B7 tumor cells were inoculated subcutaneously into the right and left flank, respectively, of NSG or BRG mice. Tumor size was assessed by caliper measurement. Before intravenous injection of T$_{CM}$, mice were total body irradiated (TBI) with one Gray (Gy; Gulmay Irradiation Cabinet). Human IL15–producing NSO cells, irradiated with 80Gy, were injected three times weekly intraperitoneally. TCR2.5D6-transduced T$_{CM}$, non-transduced T$_{CM}$, or PBS were injected in the tumor (only Supplementary Fig. S2) or intravenously (all other experiments) at indicated time points.

Conjugation and zirconium-89–labeling of aTCRmu-F(ab')$_2$

The p-isothiocanatobenzyl-derivative of desferrioxamine (DFO-Bz-NCS, Macrocyclics, Inc.) was used as a bifunctional chelator for zirconium-89 (^{89}Zr) and was added in a 3-fold molar excess to the aTCRmu-F(ab')$_2$ followed by purification using size exclusion chromatography (Sephadex G-25 M, PD10 column, GE Healthcare). The labeling of aTCRmu-F(ab')$_2$ with ^{89}Zr was performed on the basis of the protocol of Perk and colleagues (28) with slight modifications (Supplementary Material).

PET/CT imaging

Mice were anesthetized and imaged with the Inveon small-animal positron emission tomography/computer tomography (PET/CT) scanner (Siemens) after indicated time points of intravenous ^{89}Zr-aTCRmu-F(ab')$_2$ (0,7-1,5MBq corresponding to 10–20 µg) injection or 15 minutes after intravenous injection of (18-Fluor)1-Fluor-2-deoxy-D-glucose (^{18}F-FDG; 15MBq). Static PET emission images were acquired for 30 minutes (^{89}Zr-aTCRmu-F(ab')$_2$) or 20 minutes (^{18}F-FDG) and reconstructed using OSEM-3D algorithm. CT images were reconstructed using a modified Feldcamp algorithm and PET and CT images were fused and analyzed using the Inveon Research Workplace (Siemens). The data were corrected for attenuation and radioactive decay. Tracer uptake was calculated as the percentage of injected dose per gram of tissue (%ID/g, 1 cc = 1 g). For quantification, a region of interest (ROI) encompassing the tumor was drawn based on CT images, transferred to the PET data, and mean values (%ID/g) were determined using a threshold of 50% of maximal uptake inside the tumor region. For quantification of differential distribution patterns, uptake in ROI of respective tumors was analyzed without threshold and expressed as %ID/g or as total activity (%ID) by multiplying the uptake by the region volume.

Biodistribution analysis

Mice were sacrificed 48 hours after ^{89}Zr-aTCRmu-F(ab')$_2$ administration. Blood and organs were collected, weighted, and radioactivity was counted against a standard of known activity in a gamma-counter (2480Wizard2, PerkinElmer). Tumor and organ uptake was calculated as %ID/g or percent injected dose (%ID) and expressed as ratio to blood uptake.

qPCR

Genomic DNA (gDNA) was isolated using the QiAamp DNA Mini Kit (Qiagen). Part of the murinized TCR beta region (TCRb) was amplified by quantitative RT-PCR in a StepOnePlus (Applied Biosystems) as described in Supplementary Material.

Histology and IHC

During necropsy of mice, ventral and dorsal orientation of tumors was flagged by tissue ink followed by cutting the tumors in axial plane. Tumors were fixed in 10% formalin and embedded in paraffin with downward orientation of the axial cutting site. Two-micron thick sections on different levels of the tumors were stained with hematoxylin and eosin (H&E) and consecutive slides were used to detect human T cells. Anti-CD5 (4C7, Novacastra) and anti-CD3 (MRQ-39, Cell Marque) staining was performed on an automated immunostainer with an iVIEW DAB Detection Kit (Ventana Medical Systems, Roche) according to the company's protocols with slight modifications. Slides were evaluated with an Olympus BX53 microscope by semiquantitative evaluation of T-cell infiltration in predefined regions depicted by colored codes as indicated. Colocalization of imaging and histologic slices was performed by calculating the sum of total sections, including a variation factor of tissue modification due to the technical procedure.

Statistical analysis

Data are presented as mean ± SD. Statistical analysis of results was performed using GraphPad Prism software version 5.01 using the Mann–Whitney test as indicated in the figure legends.

Results

aTCRmu-F(ab')$_2$ binds specifically and with high affinity to TCR-transduced cells and binding of nonlabeled and labeled aTCRmu-F(ab')$_2$ has no impact on functionality of TCR-transgenic T$_{CM}$

The hamster aTCRmu antibody (H57-597) specifically recognizes the murine TCR beta domain present in murine T cells as well as engineered TCR constructs (22, 23, 29). We used this antibody (aTCRmu-IgG) as well as its F(ab')$_2$ fragment (aTCRmu-F(ab')$_2$) to track specifically human T cells engineered with a tumor-specific TCR (Supplementary Fig. S1). For establishment of an imaging model of TCR-transgenic T cells harboring such modification, we took advantage of the previously described human-derived leukemia-reactive TCR2.5D6 transduced into human CD8-enriched T$_{CM}$, resulting in specific recognition of a myeloperoxidase-derived peptide (MPO$_5$) in the context of HLA-B7 (23). Flow cytometry–based binding analyses using TCR2.5D6-transduced Jurkat76 cells revealed a comparable dissociation constant (K_d) for the full antibody and its F(ab')$_2$ derivate (Fig. 1A). We then analyzed the influence of aTCRmu-IgG or aTCRmu-F(ab')$_2$ on transduced T$_{CM}$. Incubation of TCR-transduced T$_{CM}$ with aTCRmu-F(ab')$_2$ for 12 hours did not influence the T-cell apoptosis rate, whereas aTCRmu-IgG induced a dose-dependent increase of apoptotic cells (Fig. 1B, top). Similarly, we detected a dose-dependent secretion of IFNγ by TCR2.5D6-transduced T$_{CM}$ after incubation with aTCRmu-IgG but not with aTCRmu-F(ab')$_2$ (Fig. 1B, bottom). To analyze the functional impact of aTCRmu-F(ab')$_2$ versus aTCRmu-IgG in vivo, T$_{CM}$ cells were transduced with TCR2.5D6 linked to the near-infrared red fluorescent protein (iRFP) and intravenously injected into NSG-mice. We found reduced percentages of engrafted TCR-transgenic T cells in different organs after intravenous application of aTCRmu-IgG, which was not observed after application of aTCRmu F(ab')$_2$ (Fig. 1C). After confir-

mation of a lack of functional influence of TCR2.5D6-transgenic T$_{CM}$ by incubation with aTCRmu-F(ab')$_2$ in vitro and in vivo, we conjugated the aTCRmu-F(ab')$_2$ with DFO-Bz-NCS followed by labeling with ^{89}Zr (^{89}Zr-aTCRmu-F(ab')$_2$) to exclude a potential functional impairment by exposure to the radioactive tracer. After in vitro labeling by ^{89}Zr-aTCRmu-F(ab')$_2$, we observed similar IFNγ secretion of labeled T$_{CM}$ in response to ML2 cells transduced with HLA-B7 (ML2-B7) as compared with incubation with the nonradioactive aTCRmu-F(ab')$_2$ (Fig. 1D).

Investigation of suitable time points for PET/CT imaging of TCR-transduced T$_{CM}$ using ^{89}Zr-aTCRmu-F(ab')$_2$

To investigate the feasibility to visualize TCR-transduced T$_{CM}$ by ^{89}Zr-aTCRmu-F(ab')$_2$ as well as determination of the optimal imaging timepoint after ^{89}Zr-aTCRmu-F(ab')$_2$ application, we developed an in vivo model of myeloid sarcoma by subcutaneous inoculation of ML2-B7 on one flank and ML2-WT cells on the other flank of BRG-mice. Transgenic T$_{CM}$ were initially directly injected in ML2-B7 tumors followed by intravenous injection of ^{89}Zr-aTCRmu-F(ab')$_2$ (Supplementary Fig. S2A). Nontransduced T$_{CM}$ were injected in ML2-WT tumors as control. In comparison with controls, we observed the strongest specific signal in the ML2-B7 tumors 48 hours after injection further confirmed by quantification of the PET signal and ex vivo biodistribution (Supplementary Fig. S2B–S2D). This time point has been therefore selected as most suitable for imaging TCR-transgenic T$_{CM}$ by ^{89}Zr-aTCRmu-F(ab')$_2$.

Investigation of dynamics of T$_{CM}$-mediated tumor rejection to determine biologically critical imaging time points in a clinically relevant ML2-based myeloid sarcoma model

To model a clinical scenario and determine biologically critical time points for T-cell imaging, we injected T$_{CM}$ intravenously into NSG mice harboring ML2 tumors as described above (Supplementary Fig. S3A). Significant rejection of ML2-B7 tumors was observed in mice injected with TCR2.5D6 T$_{CM}$ in contrast with mice treated with non-transduced T$_{CM}$ or PBS (Supplementary Fig. S3B). ML2-WT tumors showed no modification in growing kinetics following adoptive transfer of TCR-transduced T$_{CM}$ or controls (Supplementary Fig. S3B). Thus, the established model proved high efficacy of TCR2.5D6-transduced T$_{CM}$ in a clinically relevant scenario and suggested day 4 to 5 after T-cell transfer as turning point during rejection, and therefore highly interesting for imaging. Ex vivo flow cytometry analyses confirmed a significant increase in total human T cells within the ML2-B7 tumors but not in the ML2-WT tumors (Supplementary Fig. S3C). T cells were not enriched in tumors of mice injected with nontransduced T$_{CM}$, whereas T-cell infiltration was similar in spleen and lung, indicating comparable engraftment ratios (Supplementary Fig. S3C). Within the group injected with TCR2.5D6-transduced T$_{CM}$, around 30% of all T cells present in the ML2-B7 tumor was positive for aTCRmu (Supplementary Fig. S3D).

Tracking of TCR2.5D6-transduced T$_{CM}$ in tumor-bearing NSG mice by ^{89}Zr-aTCRmu-F(ab')$_2$ PET imaging in the course of tumor rejection

For monitoring of TCR2.5D6-transduced T$_{CM}$ in the established in vivo model, we applied ^{89}Zr-aTCRmu-F(ab')$_2$ 3 days after adoptive T-cell transfer of T$_{CM}$ and analyzed mice by PET/
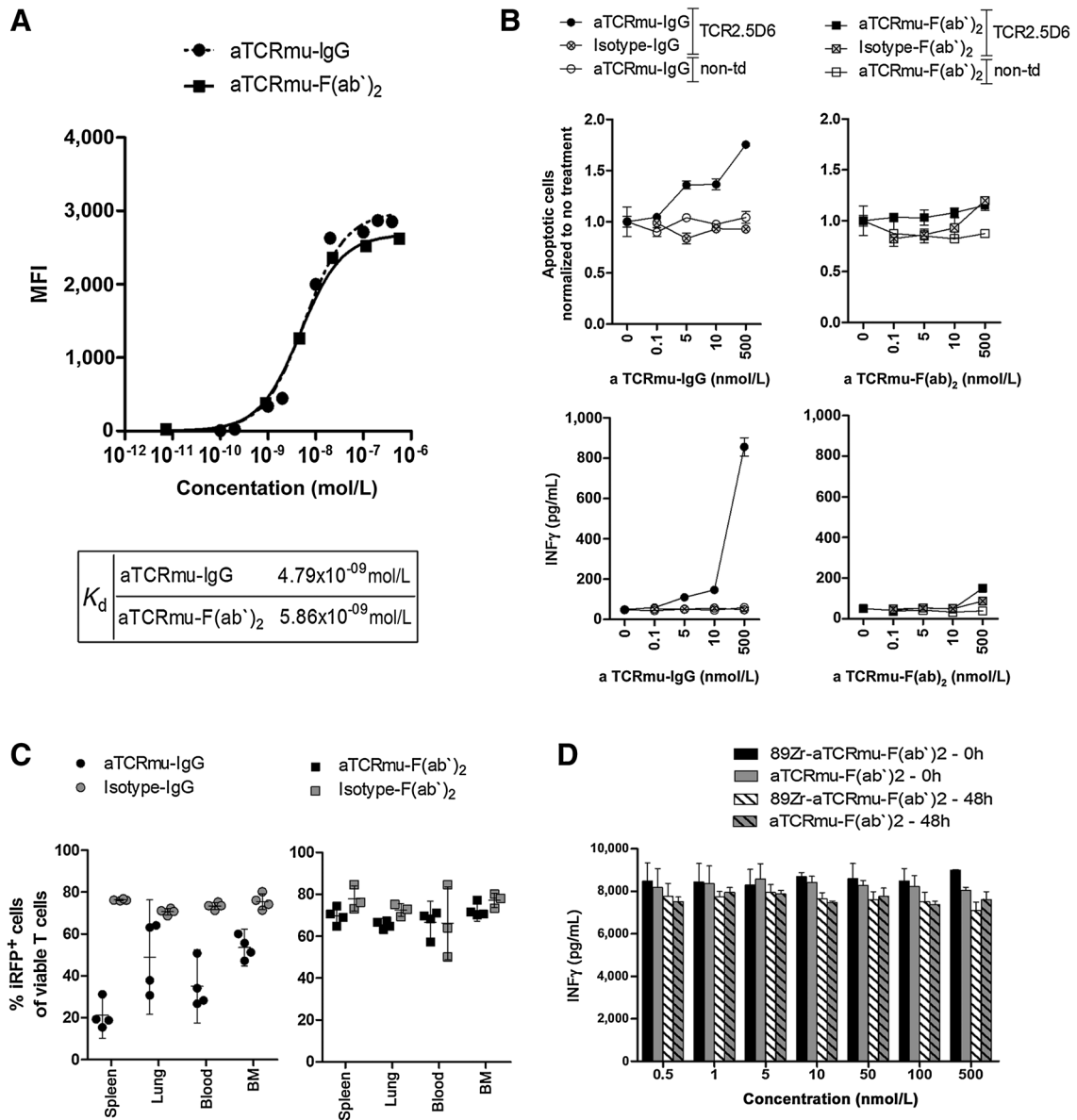
Figure 1.
Binding specificity and affinity of aTCRmu-IgG and aTCRmu-F(ab')$_2$ and their impact on function and viability of TCR2.5D6-transduced T cells. A, flow cytometry–based K_d determination of aTCRmu-IgG and aTCRmu-F(ab')$_2$ using TCR2.5D6-transduced Jurkat76 cells. Mean fluorescence intensity (MFI) values for indicated concentrations of aTCRmu-IgG or aTCRmu-F(ab')$_2$ staining and calculated K_d values for aTCRmu-IgG and F(ab')$_2$ are shown. B, apoptotic cells (top) and IFNγ secretion (bottom) of TCR2.5D6-transduced T_{CM} after 12 hours incubation with indicated concentrations of aTCRmu-IgG and isotype-IgG (left graphs) or aTCRmu-F(ab')$_2$ and isotype-F(ab')$_2$ (right graphs). Nontransduced (non-td) T_{CM} (white circles/squares) incubated with aTCRmu-IgG and aTCRmu-F(ab')$_2$ were used as additional controls. C, percentages of engrafted TCR2.5D6-iRFP-positive T cells in indicated organs of NSG mice 6 days after intravenous injection of aTCRmu-IgG and isotype-IgG (left graph) or aTCRmu-F(ab')$_2$ and isotype-F(ab')$_2$ (right graph). BM, bone marrow. Mean ± SD of %iRFP$^+$ cells of total viable (CD45$^+$CD3$^+$CD5$^+$) T cells engrafted in animals treated with aTCRmu/isotype-IgG and aTCRmu-F(ab')$_2$ ($n = 4$) and isotype-F(ab')$_2$ ($n = 3$) is shown. D, IFNγ secretion of TCR2.5D6-transduced T_{CM} after cocultivation with ML2-B7 cells is shown. Coincubation of T_{CM} and tumor cells was performed either directly (0 hours) or 48 hours after labeling with indicated concentrations of ^{89}Zr- aTCRmu-F(ab')$_2$ or nonradioactive a TCRmu-F(ab')$_2$. Mean ± SD of triplicates is depicted.

CT after 48 hours (Fig. 2A). We detected a highly distinct signal at the ML2-B7 tumor site in animals treated with TCR2.5D6-transduced T_{CM} in comparison with controls (Fig. 2B). Image-based quantification confirmed these findings (Fig. 2C). *Ex vivo* biodistribution analyses showed a 13-fold increased uptake in relation to blood in ML2-B7 tumors of mice injected with

TCR2.5D6-transduced T_{CM} (Fig. 2D). Furthermore, we detected a significant and 4-fold increased tumor-to-blood ratio in ML2-B7 tumors compared with ML2-WT tumors. Mice infused with nontransduced T_{CM} or PBS showed no differences of tumor to blood ratio between both tumors (Fig. 2D). Of note, we detected *ex vivo* a higher activity in the spleen and lung of mice
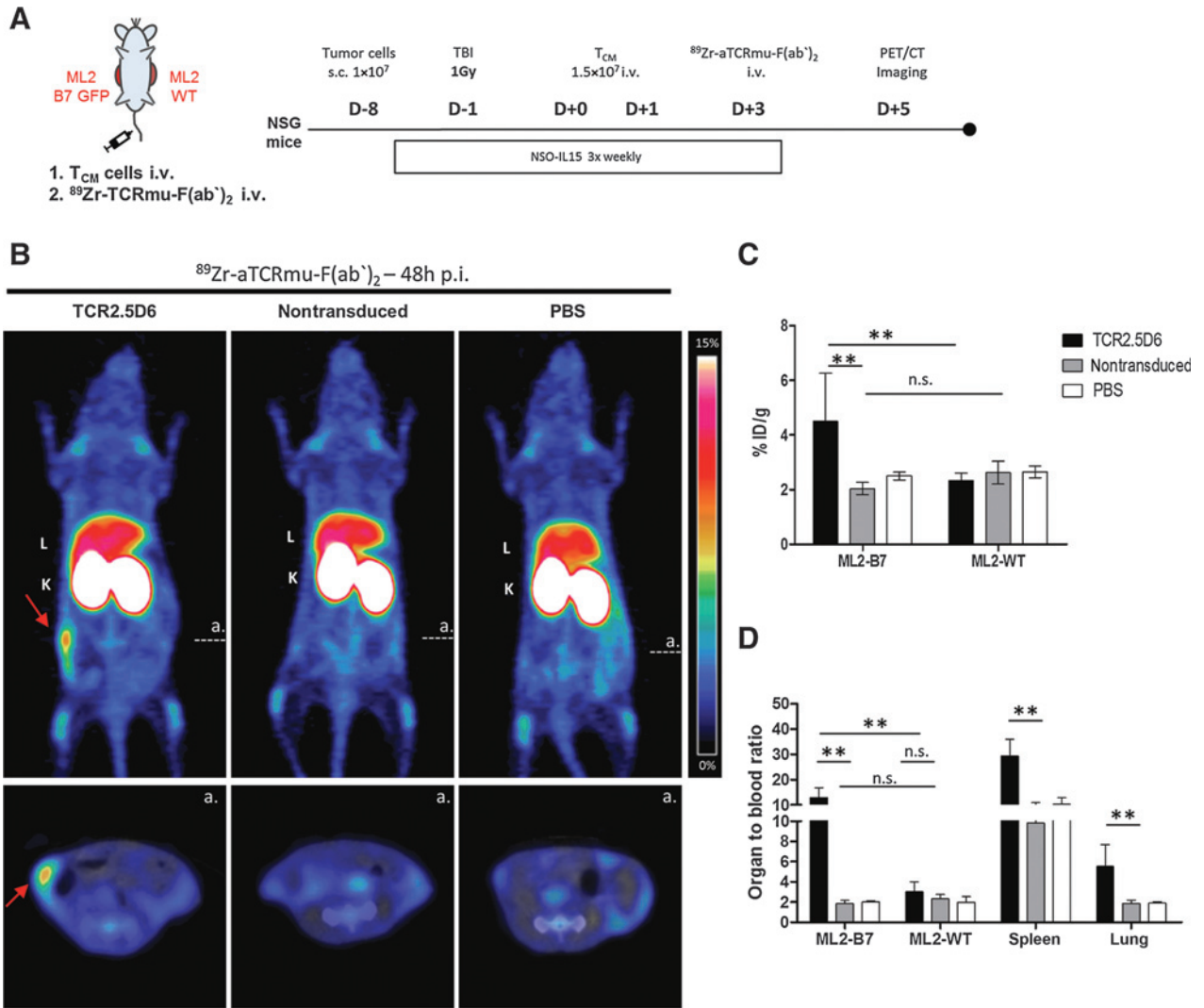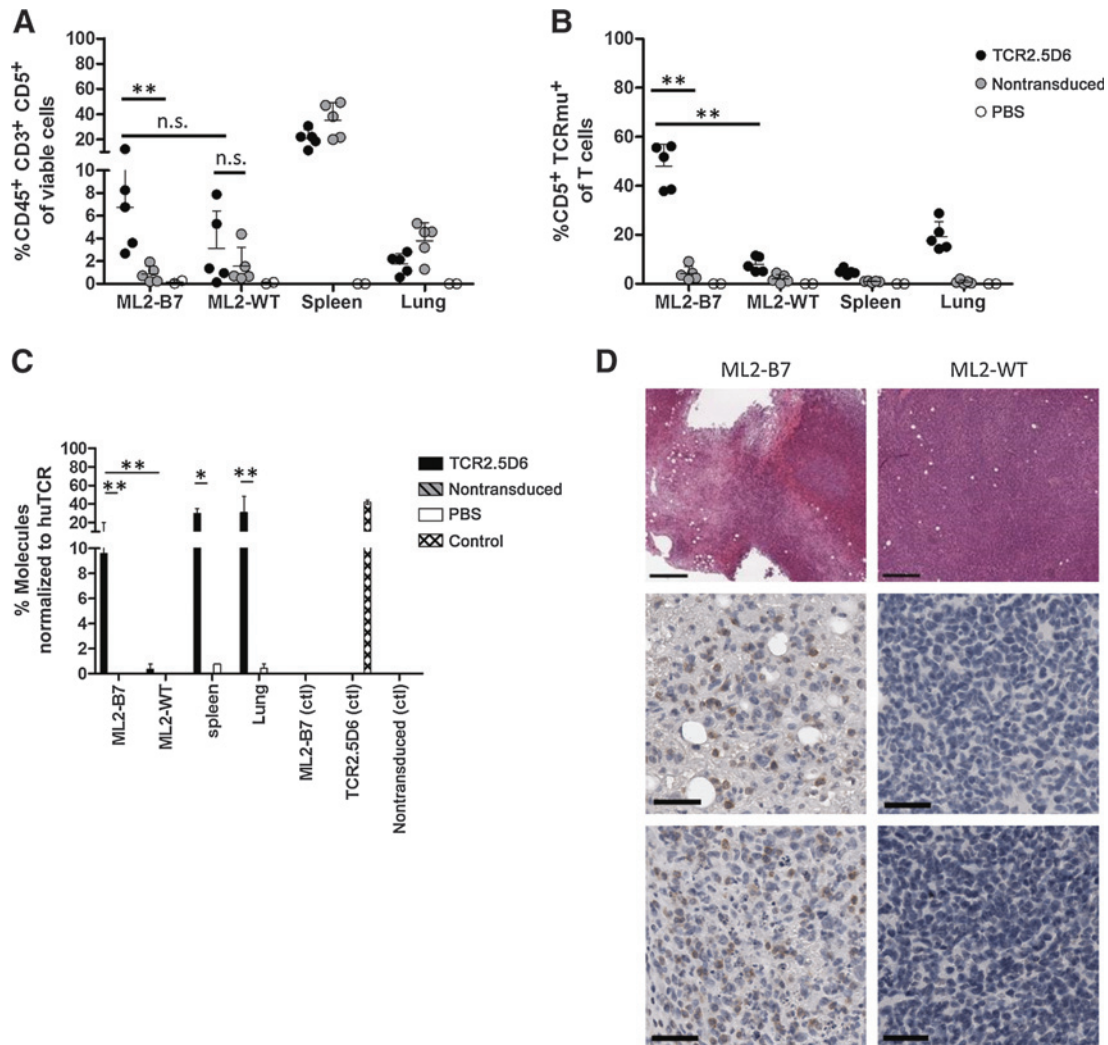
Figure 2.
Tracking of intravenously injected TCR-transduced T_{CM} within ML2-B7 tumors by ^{89}Zr-aTCRmu-F(ab')$_2$. A, overview of the experimental design. Three days after intravenous injection of T_{CM} into tumor-bearing mice, ^{89}Zr-aTCRmu-F(ab')$_2$ was injected intravenously and PET/CT imaging was performed after 48 hours. B, representative 3D-PET (MIP) and axial PET/CT images are shown. Red arrows, the signal at the ML2-B7 tumors of animals injected intravenously with TCR2.5D6-transduced T_{CM}. Dotted lines and "a" show the position of axial PET/CT images. Scale bar, 0–15%ID/g. L, liver; K, kidney. C, quantitative analysis of PET/CT images of ML2-B7 and ML2-WT tumors. Mean ± SD of %ID/g of defined ROI is depicted for $n = 5$ animals in each group treated with T_{CM} and $n = 2$ treated with PBS. D, quantitative evaluation of tumor or organ to blood ratios 48 hours after injection of ^{89}Zr-aTCRmu-F(ab')$_2$ by ex vivo biodistribution. Mean ± SD of %ID/g ratios is depicted for $n = 5$ animals in each group treated with T_{CM} and $n = 2$ treated with PBS. B–D, representative data of one of three experiments. The Mann–Whitney test: *, $P < 0.05$; **, $P < 0.01$.

treated with TCR2.5D6-transduced T_{CM} compared with non-transduced T_{CM} (Fig. 2D), whereas distribution of ^{89}Zr-aTCRmu-F(ab')$_2$ in all other organs was similar independent of the treatment modality (Supplementary Fig. S4A). Autoradiography of tumors and tissue sections confirmed these findings (Supplementary Fig. S4B). In vivo stability of aTCRmu-F(ab')$_2$ was reassured by ex vivo detection of stable ^{89}Zr-aTCRmu-F(ab')$_2$ in the blood of mice 48 hours after injection (Supplementary Fig. S4C).

We further validated our data by ex vivo detection of T cells after imaging. We observed the increased percentage of total human T cells in ML2-B7 tumors by flow cytometry in mice injected with TCR2.5D6-transduced T_{CM} (Fig. 3A). In contrast,

T-cell percentages were comparable in spleen and lung irrespective of the treatment (Fig. 3A). Moreover, we detected high percentages of TCR2.5D6-transduced T cells within the ML2-B7 tumors but not in the ML2-WT tumors (Fig. 3B) confirming the specificity of the PET-signal. Slightly enhanced levels of TCR2.5D6-transduced T cells were detected in the lung. Analysis of gDNA by qPCR revealed elevated copies of TCR2.5D6 in the ML2-B7 tumor, spleen, and lung (Fig. 3C) corresponding to biodistribution data. IHC of tumor sections showed tumor cell necrosis and presence of high numbers of CD5$^+$ T cells within ML2-B7 tumors. In contrast, we observed only few T cells in ML2-WT tumors and no signs of tumor necrosis (Fig. 3D).

Figure 3.
Presence of aTCRmu-positive T cells in ML2-B7 tumors analyzed *ex vivo* following PET/CT imaging. A and B, *ex vivo* flow-cytometry analyses of single-cell suspensions from tumors and organs 48 hours after ^{89}Zr-aTCRmu-F(ab')$_2$ injection. A and B, the percentage of viable T cells (%CD45$^+$CD3$^+$CD5$^+$; A) and of TCR2.5D6-transduced T cells (%CD5$^+$TCRmu$^+$; B) of all viable T cells is shown. Mean ± SD of mice injected with TCR2.5D6-transduced T cells ($n = 5$), nontransduced T cells ($n = 5$), and PBS ($n = 2$) is depicted. C, RT-PCR of the TCRmu gene using gDNA isolated from single cell suspension of tumors and organs. gDNA of ML2-B7 and nontransduced T$_{CM}$ served as negative control, gDNA of TCR2.5D6-transduced T$_{CM}$ as positive control. Percentage of TCRmu molecules normalized to the number of human TCR (huTCR) molecules is depicted. D, H&E staining (top) of ML2-B7 and ML2-WT tumors; bar, 400 μm. Corresponding IHC with anti-human CD5 of tumor-infiltrating T cells at two different areas of the ML2-B7 and ML2-WT tumor (middle and bottom) is shown; bar, 50 μm. A–C, the Mann–Whitney test: *, $P < 0.05$; **, $P < 0.01$.

Qualitative and quantitative evaluation of ^{89}Zr-aTCRmu-F(ab')$_2$ signals in ML2-B7 tumors

In-depth analysis of mice injected with TCR2.5D6 T$_{CM}$ revealed differences in distribution of ^{89}Zr-aTCRmu-F(ab')$_2$ within ML2-B7 tumors depending on the tumor size (Supplementary Fig. S5A). Tumors derived from different experiments ($n = 11$) were therefore classified according to their size and signal distribution pattern (Supplementary Fig. S5A–S5B). Interestingly, within the region of interest, the size correlated with the total injected activity but not with the injected activity per gram (Supplementary Fig. S5C–S5D). To confirm these observations, mice were injected subcutaneously with ML2-B7 at different time points before intravenous application of TCR2.5D6-transduced or nontransduced T$_{CM}$ application to

provide different tumor kinetics (Supplementary Fig. S6A and S6B). We primarily performed ^{18}F-FDG-PET/CT imaging and observed a homogenous uptake of ^{18}F-FDG within ML2-B7 tumors 2 days after T$_{CM}$ transfer (Fig. 4A). In contrast, ^{89}Zr-aTCRmu-F(ab')$_2$ imaging revealed again a different signal distribution with hotspot signal enhancement areas dependent on the tumor size (Fig. 4A).

We confirmed correlation of signal distribution patterns to the different groups, with group I tumors having more intense signals at the tumor border, whereas group II and III demonstrating signals in the center of the tumor (Fig. 4A). The image-based total %ID quantification in the tumor was enhanced in tumors of group I compared with group II and III (Fig. 4B) corresponding to tumor volume (Fig. 4C), whereas %ID/g of
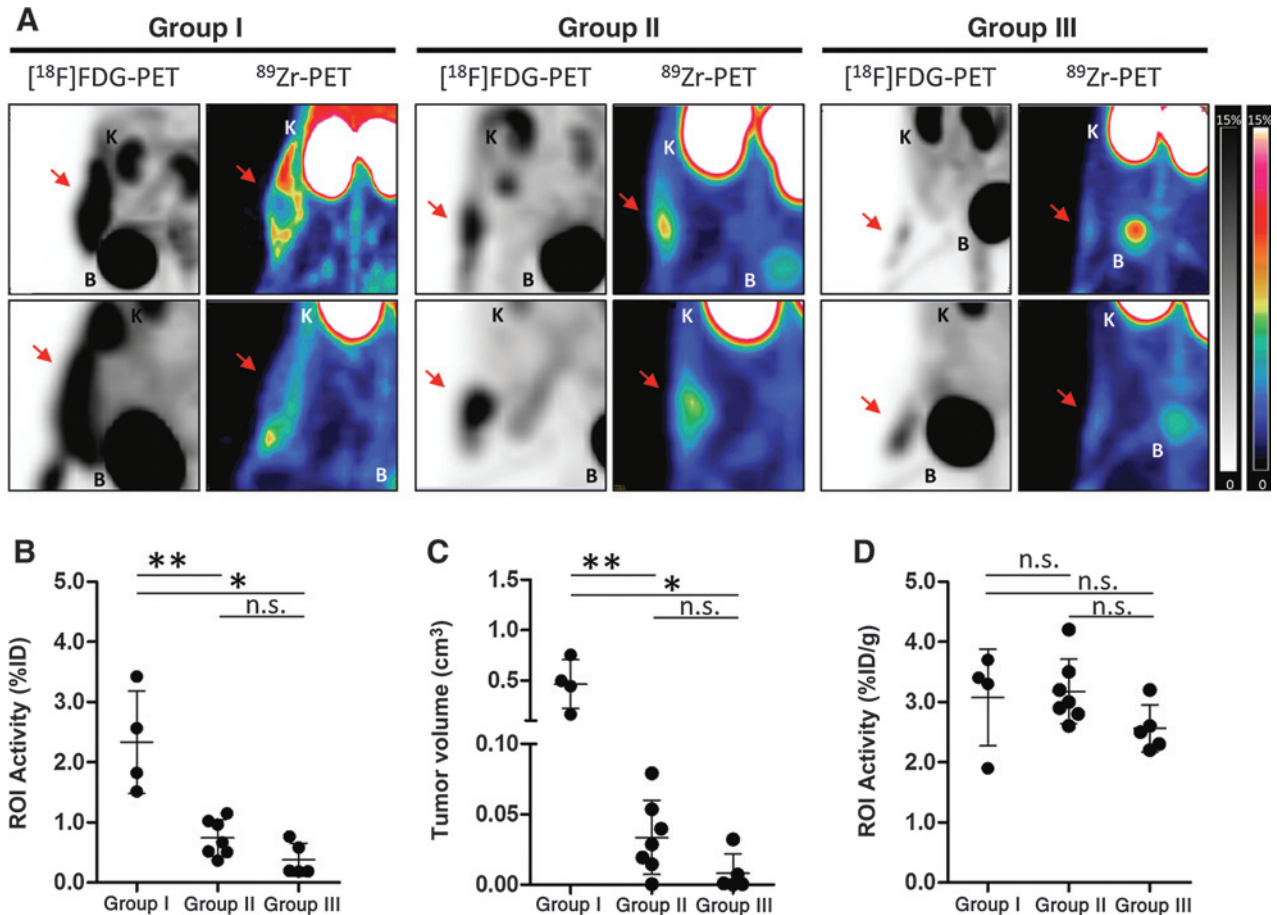
Figure 4.
Differential distribution of ^{89}Zr-aTCRmu-F(ab')$_2$ signals within ML2-B7 tumors of mice injected with TCR2.5D6-transgenic T$_{CM}$. A, representative 3D-PET (MIP) pictures of ML2-B7 tumors analyzed by ^{18}F-FDG-PET (black/white) 3 days after injection of TCR2.5D6-T$_{CM}$ and by ^{89}Zr-aTCRmu-F(ab')$_2$-PET (colored) 5 days after injection of TCR2.5D6-T$_{CM}$ (experimental design is described in Supplementary Fig. S4A). Representative data of two animals derived from group I ($n = 4$), group II ($n = 7$), and group III ($n = 5$) are shown; scale bar, 0–15%ID/g for ^{18}F-FDG and ^{89}Zr-aTCRmu-F(ab')$_2$. T, tumor; K, kidney; B, bladder. B, image-based quantitative analysis of ML2-B7 tumors according to group classification. Mean ±SD of %ID of defined ROI is depicted. C, ML2-B7 tumor volume at the day of ^{89}Zr-aTCRmu-F(ab')$_2$ imaging according to group classification is shown. Tumor volume in cm^3 determined by caliper measurement is depicted. D, quantitative analysis of PET/CT images of ML2-B7 tumors according to group classification. Mean ± SD of %ID/g of defined ROI is depicted. The Mann–Whitney test; *, $P < 0.05$; **, $P < 0.01$; n.s., nonsignificant.

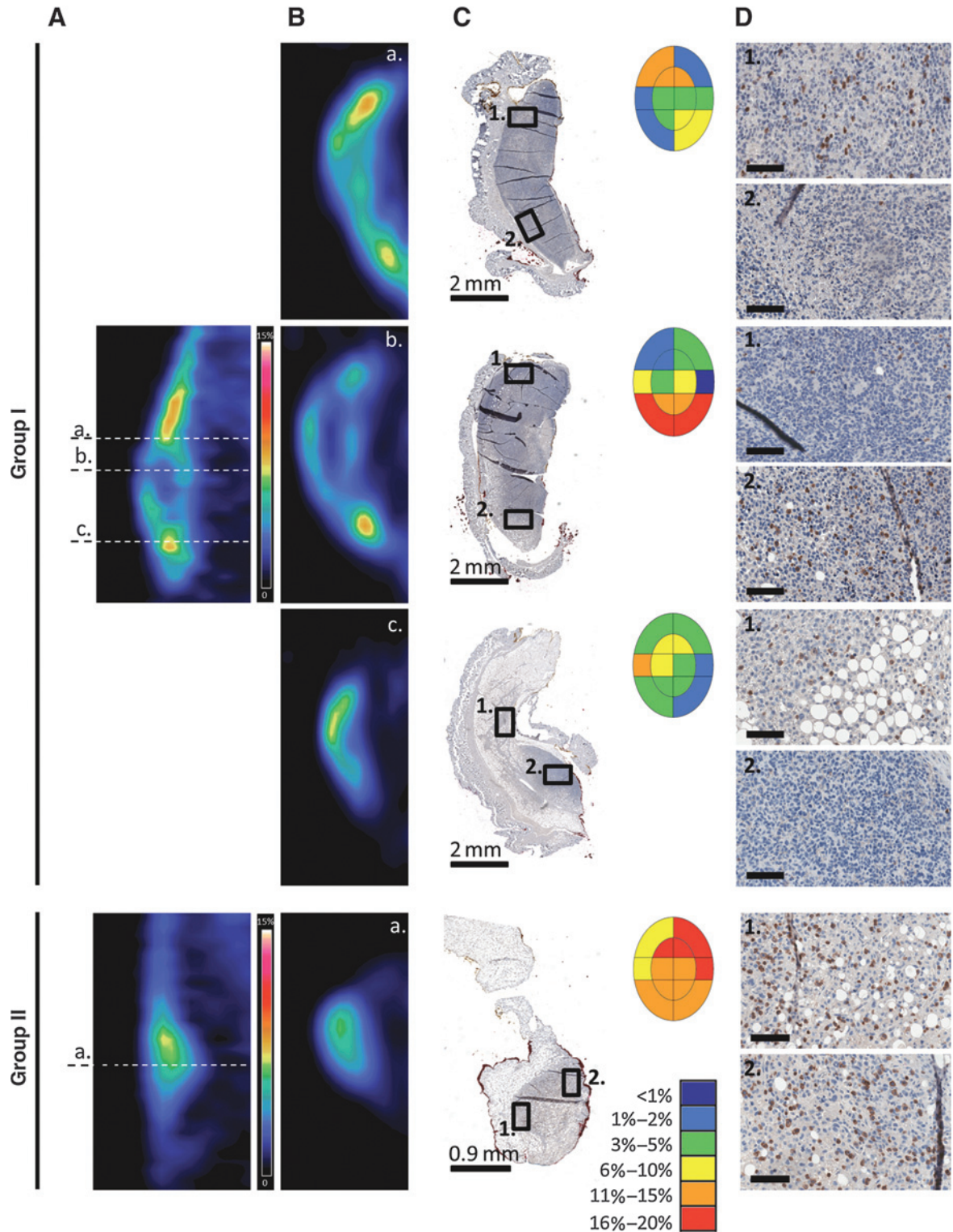tumor tissues did not show significant differences between the groups (Fig. 4D).

Mapping of adoptively transferred T cells within the tumor by ^{89}Zr-aTCRmu-F(ab')$_2$-based PET/CT

We validated the PET/CT imaging data by IHC of tumor sections on different axial levels (Fig. 5). Intra- and intersectional heterogeneity of CD3$^+$ T-cell infiltrations within tumors of group I was obvious, whereas tumors of group II showed a uniform T-cell distribution. We colocalized tumor sections to respective axial imaging levels for deeper correlation analysis (Fig. 5A–D). The intrasectional T-cell heterogeneity was mapped by semiquantitative analysis of T-cell infiltration within predefined areas correlating to respective PET-imaging levels (Fig. 5B–D). Thus, using ^{89}Zr-aTCRmu-F(ab')$_2$ PET/CT, we were able to map the differential distribution of T-cell infiltrations within the tumor, and thereby classified different tumor rejection phases reflecting the dynamics of T-cell response of TCR-transgenic T cells in this model.

Discussion

We here present a novel and highly sensitive imaging approach for mapping of TCR-engineered T cells within the tumor by PET/CT. We directly target the transgene with an antibody construct recognizing the murinized constant TCR beta domain applicable for any TCR independent of the defined specificity.

Our approach provides many advantages of previous published studies essential for clinical translation. It is, to our knowledge, the first approach using a F(ab')$_2$-based technology for specific *in vivo* imaging of human TCR-transgenic T cells by directly targeting the TCR without any impact on the function of targeted T cells. This is of particular interest as direct targeting of the TCR complex has been previously demonstrated to have an impact on T-cell function as well as viability potentially jeopardizing therapeutic efficacy (20, 30). As previously reported (22, 31–33), we also observed alterations of T-cell function and viability by the full IgG anti-TCRmu but not its

Figure 5.
T-cell imaging by PET/CT using [89]Zr-aTCRmu-F(ab')$_2$ facilitates mapping of T cells within ML2-B7 tumors of mice injected with TCR2.5D6-transgenic T$_{CM}$. A, coronal PET image of a representative ML2-B7 tumor of mice injected with TCR2.5D6 transgenic T$_{CM}$ classified into group I (top) and group II (bottom). Dotted lines, a., b., and c. show the position of corresponding axial PET images depicted in B; scale bar, 0–15%ID/g. C, heterogeneous CD3^{+} T-cell infiltration within ML2-B7 tumor sections corresponding to the respective axial PET images. IHC of CD3^{+} T cells within ML2-B7 tumor sections is depicted. Differential CD3^{+} T-cell distribution within respective tissue section was mapped by plotting the percentage of T-cell infiltration in pre-defined areas using a color code as shown in the figure; bar, 2 or 0.9 mm as shown in the figure. D, magnification of ML2-B7 tumor areas showing differential intrasectional heterogeneity of T-cell infiltration. Localization of magnification areas is shown by indicated numbers corresponding to marked areas of tumor sections shown in C; bar, 100 μm.

F(ab')$_2$. In contrast with direct *ex vivo* labeling strategies, our *in vivo* labeling approach has the major advantage to provide the capability to image at any time point of interest. This is important for long-term monitoring of the therapeutic efficacy. Moreover, by choosing the primary transgene as target for labeling usage of reporter genes can be omitted. This is of practical importance as reporter gene expression may be influenced by the metabolic stage of transgenic cells (34) and defined probes have been reported to increase background in replicating organs such as tumors, resulting in reduced sensitivity (35–37). In fact, the high sensitivity and excellent signal-to-noise ratio within the tumor observed in our experiments has not been previously reported for other T-cell imaging studies. *In vivo*, we detected an absolute uptake of 3.2% to 6.0%ID/g compared with 2.04%ID/g within the control, whereas *ex vivo* the difference was even more accentuated with 10.7%ID/g compared with 2.2%ID/g background. Imaging-based quantification has been reported to be inferior to *ex vivo* analyses due to diverse influences as detector performance, dead time, and partial volume effects as described previously (38). We additionally show that due to the heterogeneous distribution patterns of human T cells especially in large tumors, the information of uptake regarding injected dose per gram is less valuable compared with the percentage uptake of total injected dose. However, the uptake detected in our studies is still in the range of preclinical analyses of tracers demonstrated to be sufficient for clinical application (15, 39–42). Moreover, the number of effector cells infused in our experiments was within the range of those previously applied in clinical trials (1–3, 43). As T$_{CM}$ engraftment can be expected to be superior in humans as compared with NSG mice, this preclinical model may even underestimate the potential of this approach. Our technique has, therefore, the potential to be used as clinically relevant surrogate marker for efficacy of T-cell–based immunotherapies using TCR-transgenic T cells.

Specific signals detected by PET/CT were not only intensively validated by *ex vivo* biodistribution and autoradiography analyses but also by the direct detection of TCR-engineered T$_{CM}$ by flow cytometry and qPCR confirming data provided by PET/CT. Of particular interest, we were not only able to visualize T cells but concretely map them by PET/CT within the tumor as validated by corresponding IHC. The comprehensive qualitative analysis of imaging data combined with signal quantification with respect to the total injected dose therefore provided information about the stage of tumor rejection.

Background ^{89}Zr-uptake in kidney and liver was expected and results from fragment reabsorption and retention of radioactivity in these organs as described previously (44) and shown in our *in vivo* stability assays. This may limit the application for metastases affecting liver and kidneys. However, ^{89}Zr-labeling of an anti-HER2-Fab showed much better *in vivo* stability and tumor uptake compared with ^{124}I-labeling (45). There are a number of options for potential improvement as the usage of smaller constructs with rapid blood clearance (46), amino acid preloading (47), infusion of cold renal–blocking agents (48), introduction of metabolizable linkages facilitating excretion of radiometabolites (44), or infusion of DFO to capture free ^{89}Zr (49), which need to be evaluated in the future.

Potential immunogenicity of partially murinized TCR might be critical for clinical translation. Antibody development against the variable domains of a murine TCR has been previously observed in treated patients. However, this response was neither associated to the persistence of transgenic cells nor response to therapy (50). Reduction of murine gene segments sparing the relevant epitope as well as humanization of the aTCRmu-F(ab')$_2$ itself may decrease the risk of immunogenicity.

Taken together, our data indicate that this noninvasive ^{89}Zr-aTCRmu-F(ab')$_2$–based immuno-imaging technology reaches a sensitivity to provide deeper insights in pharmacodynamics of transgenic T cells with the potential for clinical translation. The technology may be useful for the timely identification of T-cell infiltration versus exclusion from the tumor and therefore might be implemented as potential surrogate marker for the identification of responders versus nonresponders.

Disclosure of Potential Conflicts of Interest

A.M. Krackhardt and R. Klar are involved in a patent application currently ongoing for the defined MPO peptide and sequences of TCR2.5D6. M. Schwaiger received a commercial research grant from Siemens Medical Research, received speakers' bureau honoraria from Siemens Lunch Symposium, and has ownership interest (including patents) in Siemens. No potential conflicts of interest were disclosed by the other authors.

Authors' Contributions

Conception and design: S. Mall, A.M. Krackhardt
Development of methodology: S. Mall, N. Yusufi, R. Wagner, R. Klar, H. Bianchi, M. Straub, M. Schwaiger, C. D'Alessandria, A.M. Krackhardt
Acquisition of data (provided animals, acquired and managed patients, provided facilities, etc.): S. Mall, N. Yusufi, R. Wagner, H. Bianchi, M. Straub, S. Audehm, I. Laitinen, M. Aichler, S. Ziegler, A.M. Krackhardt
Analysis and interpretation of data (e.g., statistical analysis, biostatistics, computational analysis): S. Mall, N. Yusufi, R. Wagner, H. Bianchi, K. Steiger, M. Straub, I. Laitinen, M. Aichler, S. Ziegler, M. Mustafa, M. Schwaiger, C. D'Alessandria, A.M. Krackhardt
Writing, review, and/or revision of the manuscript: S. Mall, N. Yusufi, I. Laitinen, M. Aichler, C. Peschel, S. Ziegler, M. Mustafa, M. Schwaiger, C. D'Alessandria, A.M. Krackhardt
Administrative, technical, or material support (i.e., reporting or organizing data, constructing databases): S. Mall, K. Steiger, I. Laitinen, M. Schwaiger, A.M. Krackhardt
Study supervision: M. Schwaiger, A.M. Krackhardt

Acknowledgments

Grant Support

References

1. Johnson LA, Morgan RA, Dudley ME, Cassard L, Yang JC, Hughes MS, et al. Gene therapy with human and mouse T-cell receptors mediates cancer regression and targets normal tissues expressing cognate antigen. Blood 2009;114:535–46.

2. Robbins PF, Morgan RA, Feldman SA, Yang JC, Sherry RM, Dudley ME, et al. Tumor regression in patients with metastatic synovial cell sarcoma and melanoma using genetically engineered lymphocytes reactive with NY-ESO-1. J Clin Oncol 2011;29:917–24.

3. Morgan RA, Dudley ME, Wunderlich JR, Hughes MS, Yang JC, Sherry RM, et al. Cancer regression in patients after transfer of genetically engineered lymphocytes. Science 2006;314:126–9.

4. Robbins PF, Kassim SH, Tran TL, Crystal JS, Morgan RA, Feldman SA, et al. A pilot trial using lymphocytes genetically engineered with an NY-ESO-1-reactive T-cell receptor: long-term follow-up and correlates with response. Clin Cancer Res 2015;21:1019–27.

5. Dobrenkov K, Olszewska M, Likar Y, Shenker L, Gunset G, Cai S, et al. Monitoring the efficacy of adoptively transferred prostate cancer-targeted human T lymphocytes with PET and bioluminescence imaging. J Nucl Med 2008;49:1162–70.

6. Griessinger CM, Kehlbach R, Bukala D, Wiehr S, Bantleon R, Cay F, et al. In vivo tracking of Th1 cells by PET reveals quantitative and temporal distribution and specific homing in lymphatic tissue. J Nucl Med 2014;55:301–7.

7. Adonai N, Nguyen KN, Walsh J, Iyer M, Toyokuni T, Phelps ME, et al. Ex vivo cell labeling with 64Cu-pyruvaldehyde-bis(N4-methylthiosemicarbazone) for imaging cell trafficking in mice with positron-emission tomography. Proc Natl Acad Sci U S A 2002;99:3030–5.

8. Eriksson O, Sadeghi A, Carlsson B, Eich T, Lundgren T, Nilsson B, et al. Distribution of adoptively transferred porcine T-lymphoblasts tracked by (18)F-2-fluoro-2-deoxy-D-glucose and position emission tomography. Nucl Med Biol 2011;38:827–33.

9. Botti C, Negri DR, Seregni E, Ramakrishna V, Arienti F, Maffioli L, et al. Comparison of three different methods for radiolabelling human activated T lymphocytes. Eur J Nucl Med 1997;24:497–504.

10. Bhatnagar P, Li Z, Choi Y, Guo J, Li F, Lee DY, et al. Imaging of genetically engineered T cells by PET using gold nanoparticles complexed to Copper-64. Integr Biol 2013;5:231–8.

11. Shu CJ, Radu CG, Shelly SM, Vo DD, Prins R, Ribas A, et al. Quantitative PET reporter gene imaging of CD8+T cells specific for a melanoma-expressed self-antigen. Int Immunol 2009;21:155–65.

12. Doubrovin MM, Doubrovina ES, Zanzonico P, Sadelain M, Larson SM, O'Reilly RJ. In vivo imaging and quantitation of adoptively transferred human antigen-specific T cells transduced to express a human norepinephrine transporter gene. Cancer Res 2007;67:11959–69.

13. Penheiter AR, Russell SJ, Carlson SK. The sodium iodide symporter (NIS) as an imaging reporter for gene, viral, and cell-based therapies. Curr Gene Ther 2012;12:33–47.

14. McCracken MN, Vatakis DN, Dixit D, McLaughlin J, Zack JA, Witte ON. Noninvasive detection of tumor-infiltrating T cells by PET reporter imaging. J Clin Invest 2015;125:1815–26.

15. Yaghoubi SS, Jensen MC, Satyamurthy N, Budhiraja S, Paik D, Czernin J, et al. Noninvasive detection of therapeutic cytolytic T cells with 18F-FHBG PET in a patient with glioma. Nat Clin Pract Oncol 2009;6:53–8.

16. Pandit-Taskar N, O'Donoghue JA, Beylergil V, Lyashchenko S, Ruan S, Solomon SB, et al. (8)(9)Zr-huJ591 immuno-PET imaging in patients with advanced metastatic prostate cancer. Eur J Nucl Med Mol Imaging 2014; 41:2093–105.

17. Kanwar B, Gao DW, Hwang AB, Grenert JP, Williams SP, Franc B, et al. In vivo imaging of mucosal CD4+ T cells using single photon emission computed tomography in a murine model of colitis. J Immunol Methods 2008;329:21–30.

18. Tavare R, McCracken MN, Zettlitz KA, Knowles SM, Salazar FB, Olafsen T, et al. Engineered antibody fragments for immuno-PET imaging of endogenous CD8+ T cells in vivo. Proc Natl Acad Sci U S A 2014;111:1108–13.

19. Tavare R, McCracken MN, Zettlitz KA, Salazar FB, Olafsen T, Witte ON, et al. Immuno-PET of murine T-cell reconstitution postadoptive stem cell transplantation using anti-CD4 and anti-CD8 Cys-diabodies. J Nucl Med 2015;56:1258–64.

20. Griessinger CM, Maurer A, Kesenheimer C, Kehlbach R, Reischl G, Ehrlichmann W, et al. 64Cu antibody-targeting of the T-cell receptor and

21. Cohen CJ, Zhao Y, Zheng Z, Rosenberg SA, Morgan RA. Enhanced anti-tumor activity of murine-human hybrid T-cell receptor (TCR) in human lymphocytes is associated with improved pairing and TCR/CD3 stability. Cancer Res 2006;66:8878–86.

22. Kubo RT, Born W, Kappler JW, Marrack P, Pigeon M. Characterization of a monoclonal antibody which detects all murine alpha beta T-cell receptors. J Immunol 1989;142:2736–42.

23. Klar R, Schober S, Rami M, Mall S, Merl J, Hauck SM, et al. Therapeutic targeting of naturally presented myeloperoxidase-derived HLA peptide ligands on myeloid leukemia cells by TCR-transgenic T cells. Leukemia 2014;28:2355–66.

24. Liang X, Weigand LU, Schuster IG, Eppinger E, van der Griendt JC, Schub A, et al. A single TCR alpha-chain with dominant peptide recognition in the allorestricted HER2/neu-specific T-cell repertoire. J Immunol 2010; 184:1617–29.

25. Weigand LU, Liang X, Schmied S, Mall S, Klar R, Stotzer OJ, et al. Isolation of human MHC class II-restricted T cell receptors from the autologous T-cell repertoire with potent anti-leukaemic reactivity. Immunology 2012;137: 226–38.

26. Wang X, Berger C, Wong CW, Forman SJ, Riddell SR, Jensen MC. Engraftment of human central memory-derived effector CD8+ T cells in immunodeficient mice. Blood 2011;117:1888–98.

27. Heemskerk MH, Hoogeboom M, de Paus RA, Kester MG, van der Hoorn MA, Goulmy E, et al. Redirection of antileukemic reactivity of peripheral T lymphocytes using gene transfer of minor histocompatibility antigen HA-2-specific T-cell receptor complexes expressing a conserved alpha joining region. Blood 2003;102:3530–40.

28. Perk LR, Vosjan MJ, Visser GW, Budde M, Jurek P, Kiefer GE, et al. p-Isothiocyanatobenzyl-desferrioxamine: a new bifunctional chelate for facile radiolabeling of monoclonal antibodies with zirconium-89 for immuno-PET imaging. Eur J Nucl Med Mol Imaging 2010;37:250–9.

29. Kuball J, Hauptrock B, Malina V, Antunes E, Voss RH, Wolfl M, et al. Increasing functional avidity of TCR-redirected T cells by removing defined N-glycosylation sites in the TCR constant domain. J Exp Med 2009; 206:463–75.

30. Carpenter PA, Pavlovic S, Tso JY, Press OW, Gooley T, Yu XZ, et al. Non-Fc receptor-binding humanized anti-CD3 antibodies induce apoptosis of activated human T cells. J Immunol 2000;165:6205–13.

31. Drobyski WR, Majewski D. Treatment of donor mice with an alpha beta T-cell receptor monoclonal antibody induces prolonged T-cell nonresponsiveness and effectively prevents lethal graft-versus-host disease in murine recipients of major histocompatibility complex (MHC)-matched and MHC-mismatched donor marrow grafts. Blood 1996;87:5355–69.

32. Nishimura Y, Eto M, Maeda T, Hiromatsu K, Kobayashi N, Nomoto K, et al. Inhibition of skin xenograft rejection by depleting T-cell receptor alpha beta-bearing cells without T-cell receptor gamma delta-bearing cells or natural killer cells by monoclonal antibody. Immunology 1994;83:196–204.

33. Kummer U, Zengerle U, Pischel J, Trautmann B, Mailhammer R, Sidell N. Increased in vivo mitogenicity of anti-TCR/CD3 monoclonal antibody through reduced interaction with Fcgamma receptors. Immunol Lett 2001;75:153–8.

34. Shu CJ, Guo S, Kim YJ, Shelly SM, Nijagal A, Ray P, et al. Visualization of a primary anti-tumor immune response by positron emission tomography. Proc Natl Acad Sci U S A 2005;102:17412–7.

35. Jadvar H, Yap LP, Park R, Li Z, Chen K, Hughes L, et al. [18F]-2′-Fluoro-5-methyl-1-beta-D-arabinofuranosyluracil (18F-FMAU) in prostate cancer: initial preclinical observations. Mol Imaging 2012;11:426–32.

36. Tehrani OS, Muzik O, Heilbrun LK, Douglas KA, Lawhorn-Crews JM, Sun H, et al. Tumor imaging using 1-(2′-deoxy-2′-18F-fluoro-beta-D-arabino-furanosyl)thymine and PET. J Nucl Med 2007;48:1436–41.

37. McCracken MN, Radu CG. Targeted noninvasive imaging of the innate immune response. Proc Natl Acad Sci U S A 2015;112:5868–9.

38. Mannheim JG, Judenhofer MS, Schmid A, Tillmanns J, Stiller D, Sossi V, et al. Quantification accuracy and partial volume effect in dependence of the attenuation correction of a state-of-the-art small animal PET scanner. Phys Med Biol 2012;57:3981–93.

subsequent internalization enables in vivo tracking of lymphocytes by PET. Proc Natl Acad Sci U S A 2015;112:1161–6.

39. Stelter L, Amthauer H, Rexin A, Pinkernelle J, Schulz P, Michel R, et al. An orthotopic model of pancreatic somatostatin receptor (SSTR)-positive tumors allows bimodal imaging studies using 3T MRI and animal PET-based molecular imaging of SSTR expression. Neuroendocrinology 2008;87:233–42.

40. Borjesson PK, Jauw YW, de Bree R, Roos JC, Castelijns JA, Leemans CR, et al. Radiation dosimetry of 89Zr-labeled chimeric monoclonal antibody U36 as used for immuno-PET in head and neck cancer patients. J Nucl Med 2009;50:1828–36.

41. Pandit-Taskar N, O'Donoghue J, Martinez D, Lyashchenko S, Carrasquillo J, Durack J, et al. First in Human 89Zr-Df-IAB2M anti-prostate specific membrane antigen (PSMA) minibody in patients with metastatic prostate cancer. J Nucl Med 2015;56(supplement 3):400.

42. Viola-Villegas NT, Sevak KK, Carlin SD, Doran MG, Evans HW, Bartlett DW, et al. Noninvasive Imaging of PSMA in prostate tumors with (89)Zr-Labeled huJ591 engineered antibody fragments: the faster alternatives. Mol Pharm 2014;11:3965–73.

43. Chodon T, Comin-Anduix B, Chmielowski B, Koya RC, Wu Z, Auerbach M, et al. Adoptive transfer of MART-1 T-cell receptor transgenic lymphocytes and dendritic cell vaccination in patients with metastatic melanoma. Clin Cancer Res 2014;20:2457–65.

44. Arano Y. Strategies to reduce renal radioactivity levels of antibody fragments. Q J Nucl Med 1998;42:262–70.

45. Mendler CT, Gehring T, Wester HJ, Schwaiger M, Skerra A. 89Zr-Labeled versus 124I-labeled alphaHER2 Fab with optimized plasma half-life for high-contrast tumor imaging in vivo. J Nucl Med 2015; 56:1112–8.

46. Holliger P, Hudson PJ. Engineered antibody fragments and the rise of single domains. Nat Biotechnol 2005;23:1126–36.

47. van Eerd JE, Vegt E, Wetzels JF, Russel FG, Masereeuw R, Corstens FH, et al. Gelatin-based plasma expander effectively reduces renal uptake of 111In-octreotide in mice and rats. J Nucl Med 2006;47:528–33.

48. Samaniego F, Berkova Z, Romaguera JE, Fowler N, Fanale MA, Pro B, et al. 90Y-ibritumomab tiuxetan radiotherapy as first-line therapy for early stage low-grade B-cell lymphomas, including bulky disease. Br J Haematol 2014;167:207–13.

49. Abou DS, Ku T, Smith-Jones PM. In vivo biodistribution and accumulation of 89Zr in mice. Nucl Med Biol 2011;38:675–81.

50. Davis JL, Theoret MR, Zheng Z, Lamers CH, Rosenberg SA, Morgan RA. Development of human anti-murine T-cell receptor antibodies in both responding and nonresponding patients enrolled in TCR gene therapy trials. Clin Cancer Res 2010;16:5852–61.